Chapter 5

Inner Detectors

5.1 Silicon System Overview

The PHENIX multiplicity and vertex detector (MVD) provides event characterization, a centrality trigger, the collision vertex position along the beams, and the measurement of fluctuations in the charged particle distributions. The system has silicon strip detectors arranged in two concentric barrels around the beam pipe in the center of PHENIX, and endcaps consisting of a single layer of silicon pad detectors. The total area of silicon is approximately 0.5 m^2. Both pad and strip detectors are single sided and are read out with identical front end electronics mounted on hybrid circuits. The pulse height from each strip or pad is transferred to the data acquisition system via optical fiber links. The total silicon channel count is 34,816.

The central barrels have radii of 5 and 8 cm and lenghts of 64 cm. The single-event coverage about midrapidity is five units in η for the inner barrel layer and four units for the outer layer; however, the η coverage for event-averaged quantities is extended due to the variation of the vertex position along the direction of the colliding beams. The inner and outer barrels are composed of silicon strip detector wafers, with an area of 5×7 cm^2 and 5×7.5 cm^2, respectively. The strips have a pitch of 200 μm and are oriented perpendicularly to the beam. Each barrel layer has six azimuthal sectors, and the two barrel layers are mounted on a common support structure made of Rohacell foam.

The disk shaped end caps, which comprise pads ranging in size from approximately 2×2 to 5×5 mm^2, are positioned in z at -35 and $+35$ cm. The pseudorapidity coverage is 2.7 for a single event occurring at $z = 0$. The η segmentation is more than adequate for fluctuation studies, and pulse height analysis allows the unfolding of multiple hits in one pad. The azimuthal segmentation, along with the full azimuthal coverage, makes it possible to look for fluctuations in two dimensions. The highest channel occupancies for central events are 0.35–0.46 for $dN_{ch}/d\eta = 1000$.

The vertex position can be located using hits in the barrel for z position between -40 and $+40$ cm, which covers the 2σ length of the interaction region. The multiplicity trigger is formed using the sum of silicon channels (both pads and strips) above a threshold corresponding to approximately 0.25–0.33 of a minimum ionizing particle (mip). This threshold will be tuned to optimize the trigger performance, and a rather low threshold will be used for zero suppression in the data stream.

The front-end electronics are optimized for minimum size, power dissipation and cost, while the design allows for the unfolding of multiple particle hits in each silicon pixel. The dynamic range is 8 mips, and the signal to noise better than 10:1 for a single mip. The shaping time of the preamplifier is 50–60 ns, limited by the bunch crossing time to avoid pileup in p + p collisions and allow use of the silicon in the LVL-1 trigger. Alhough the multiplicity in a single Au + Au collision is very high, the expected luminosity at RHIC is such that special considerations of radiation hardness for either the detectors or the front end electronics is not required [1].

5.2 Silicon System Changes

Design work after the CDR has resulted in a number of changes in the silicon detector coverage, mechanical structures, cooling system, and front end electronics, which include:

1. Removal of a large portion of the central silicon detectors in the upper two thirds of the outer barrel layer.
2. Progress in the design of the front-end electronics and hybrid circuit for the MVD, making them more similar to the rest of PHENIX, lowering the cost, and improving the applicability of the design to other experiments.
3. Relocation of the LVL-1 trigger to outside the silicon enclosure and concentration of the electronics below the detector.
4. Extensive studies and tests of air cooling the MVD, which would lower the cost and minimize material in the path of the particles, and would elminate the possiblitity of any coolant spills in the region of the silicon.

The most significant changes have been driven by detailed studies of electrons arising from photon conversions in the MVD. These studies have been made using PISA to integrate the MVD with the magnetic field, the central arms, and other sources of conversion electrons in PHENIX. Details of this simulation are presented in Chapter 3. This approach allowed a careful study of the tradeoff between large silicon coverage to maximize the vertex finding efficiency in low multiplicity events, and reduction of the material to minimize photon conversions in high multiplicity events. The optimum solution to these competing requirements was achieved by removing a large portion of the central silicon detectors from the upper two-thirds of the outer barrel layer, and concentrating the electronics as far from the MVD as possible at the bottom of the detector support carriages. Removal of the silicon from only one barrel layer preserves the triggering capability, and the coverage for the multiplicity and fluctuation measurement.

The updated geometry is shown in Fig. 5.1. The consequences of these changes to channel counts, mechanical design, and cooling requirements are detailed in the mechanical design

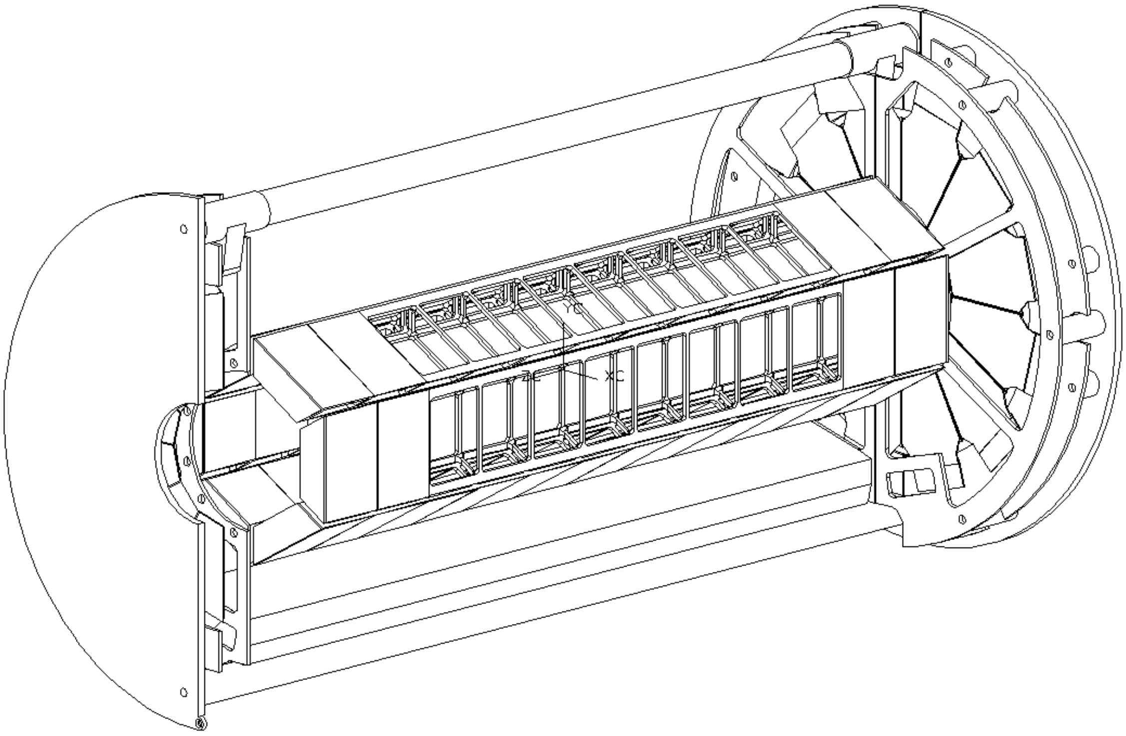

Figure 5.1: Layout of silicon detectors in the MVD.

section below; the simulation results quantifying the tradeoff and leading to these design changes are presented in the performance section; and the improved desgin for the front-end electronics and hybrid circuit are described in the electronics section.

5.3 Mechanical

5.3.1 Silicon detectors

The inner barrel consists of silicon detector wafers with an area of 5.3×5.0 cm^2, and the outer barrel uses two different wafers with an area of 5.3×7.0 cm^2 and 5.3×7.5 cm^2. The maximum size possible varies somewhat with the detector supplier; we will make the choice of supplier and finalize this geometry issue in the next year. The strip pitch on both detector sizes is 200 μm, yielding 256 channels per detector. The silicon detectors are arranged in six azimuthal sectors consisting of 12 detector wafers along the beam direction. The PISA studies described in more detail below resulted in the removal of the 8 central wafers in top four sectors of the outer barrel. This is shown in Fig. 5.1.

Each pad endcap is still composed of 12 "sectors", with each "sector" being manufactured from one 4-in. wafer. The inner radius is 5 cm and the outer radius is 12 cm. There have been no changes made to the silicon pad detectors or layouts. We are, however, currently

Table 5.1: Silicon Detector Channel Count

Detector Type	Size (cm^2)	ϕ sectors	z sectors	Total Channels
Inner Barrel	5.3×5.0	6	12	18,432
Outer Barrel	5.3×7.5	2	12	6144
Outer Barrel	5.3×7.5	4	4	4096
End Cap	6.3×7.0	12	2	6144
Total				34,816

investigating the possibility of having detectors with double metallization layers. This would bring traces from the pads out to the edge of the detector, and allow wire bonding directly to the front end electronics with a much simpler kapton cable.

The detector types and the updated number of wafers, and channel counts are summarized in Table 5.1.

5.3.2 Support Structures

The support structure for the MVD must use a minimum of material thickness to prevent background from photon conversions, but it must also be rigid to sopport and protect the silicon inside. The MVD will reside inside an enclosure, which opens in a "clam-shell" fashion to allow installation around the beam pipe. Each half-cylinder consists of aluminum endplates, with two graphite composite struts to connect and support them. The endplates mount to the magnet with graphite composite struts, and upon installation are brought together to form a complete cylinder. The cylinder is supported from one magnet pole face and held with a spring-loaded bar to the other pole face to provide vibrational isolation. The endplates are separate from the motherboards for the silicon pad detectors, which are located inside of the support endplates. This arrangement is shown in Fig. 5.2.

The half-cylinders have an enclosure of Rohacell foam, covered on each side with aluminized mylar, to provide environmental isolation of the MVD and mechanical protection. Such an enclosure allows the electronics to be cooled with air below the ambient temperature of the experimental hall, if necessary. The enclosure also electrically shields the detectors and front end electronics from the other elements of PHENIX to reduce pickup of noise. The aluminized mylar layers can also be held at a fixed potential, should additional shielding be necessary.

The silicon pad detector endcaps are mounted to a G-10, or polyimide/fiber circuit board for better CTE match, motherboard that supports both the detectors and the hybrid circuits and provides DC power. The motherboards are mounted to the endplates, and have cutouts to allow standoff bars for mounting the central barrel support structure. These structural elements are shown in Fig. 5.2.

The barrel detector wafers are supported on Rohacell cages as described in the CDR. We are investigating the machining properties of the Rohacell foam to determine what fraction

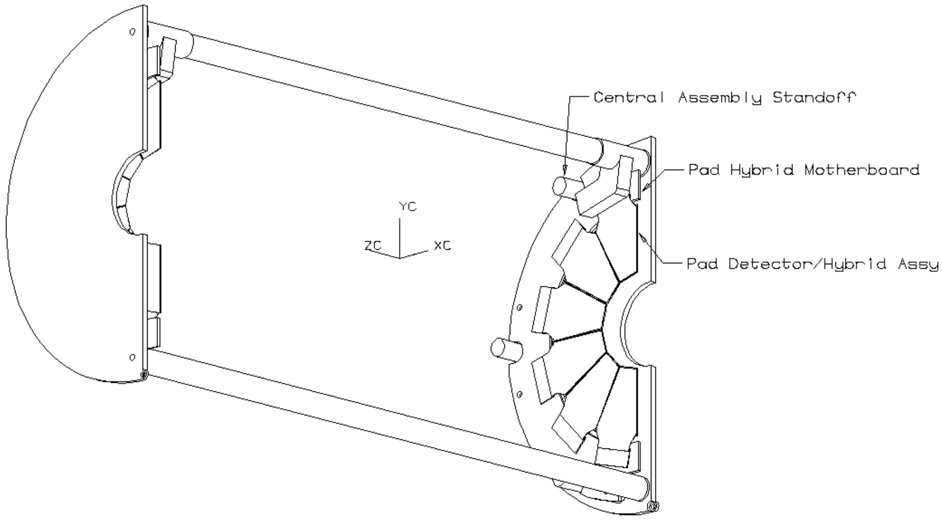

Figure 5.2: Cutaway view of the silicon support and enclosure half-cylinders.

of an azimuthal sector may be machined in one piece. We would like to fabricate an entire sector to eliminate the need for glue joints in the Rohacell. Finite element analysis of the azimuthal sector structure has shown that the graphite epoxy stiffener bars described in the CDR are unnecessary due to the structural strength provided by the silicon detectors glued to the Rohacell. We will investigate the effect of omitting some of the outer silicon detectors on this conclusion.

The azimuthal sectors are mounted to an adapter plate bolted to standoff bars on the enclosure endplate. This is a thin plate with large cutouts, as shown in Fig. 5.3, fabricated from G-10 or a graphite epoxy sheet. The design of this structure is constrained by the requirement of minimizing the amount of material in front of the silicon pads. The exact geometry and thickness of this piece is still being optimized.

The PISA studies described below show that the background of conversion electrons from the MVD is smaller when the hybrid circuits are located as far from the electron arms as possible in azimuth. To enter the electron arm, the path of the electrons must be significantly curved by the magnetic field. For a larger distance in azimuth the required bend becomes larger, implying softer electrons captured into the electron arm acceptance. Maximizing this distance results in accepting electrons which fall mostly below the angular acceptance cutoff of the ring imaging Cherenkov counter (RICH). Consequently, we have modified the mounting scheme of the electronics to concentrate them at the bottom of the barrel, as shown in Figs. 5.1,5.4. The electronics are radially as far from the vertex as possible within the MVD radial distance allotment. This helps with rejection of background electrons and allows use of the graphite composite enclosure struts to help support the electronics packages (Fig. 5.5). We have determined that the resulting length increase of the kapton cables is acceptable; the capacitance is still low enough for good preamplifier signal to noise performance.

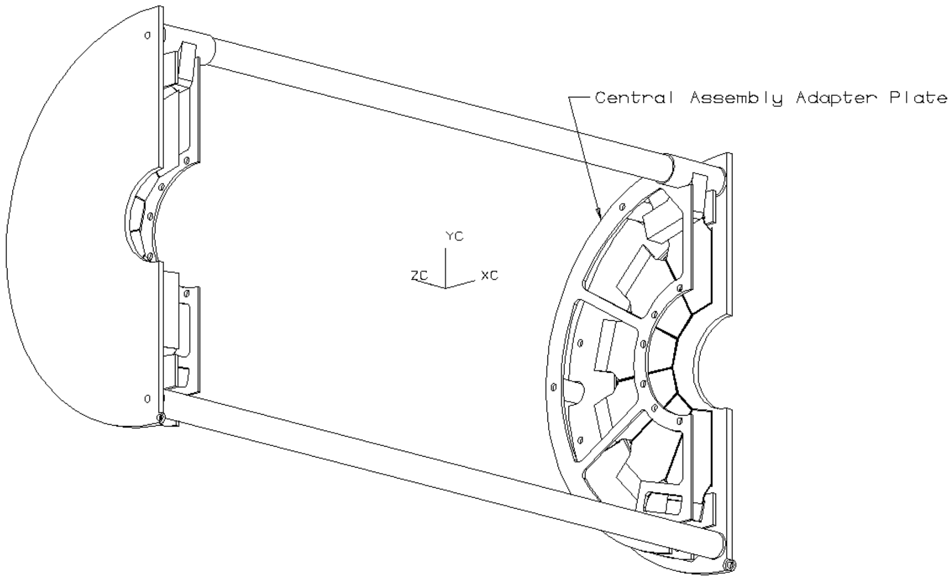

Figure 5.3: Silicon enclosure with adapter plate for central assembly.

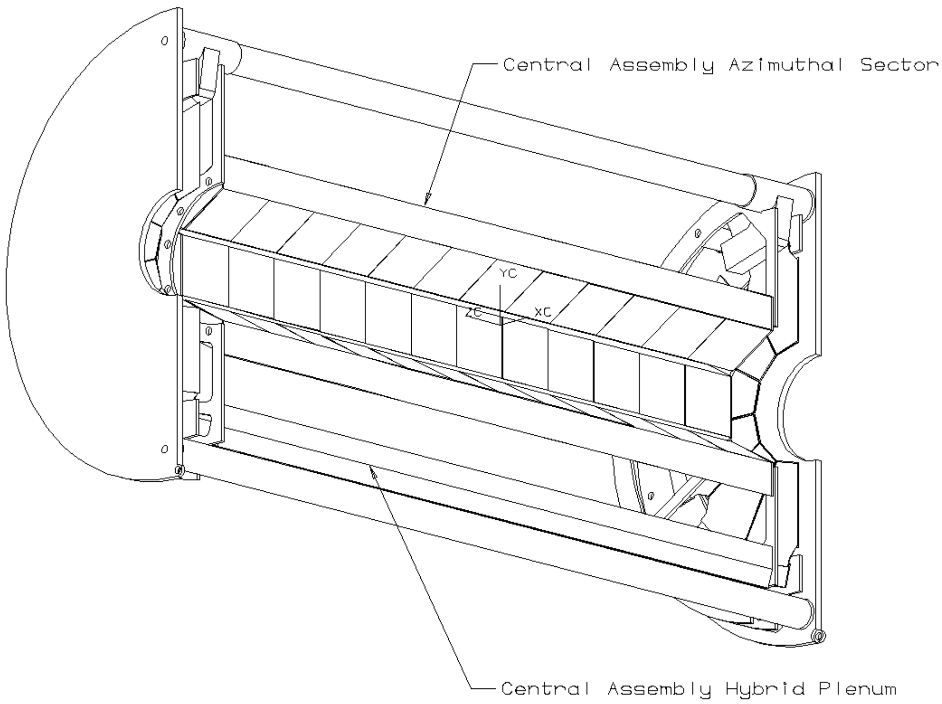

Figure 5.4: Cutaway view of the silicon enclosure, showing the central barrel assembly and plenum enclosure. Cables are omitted for clarity.

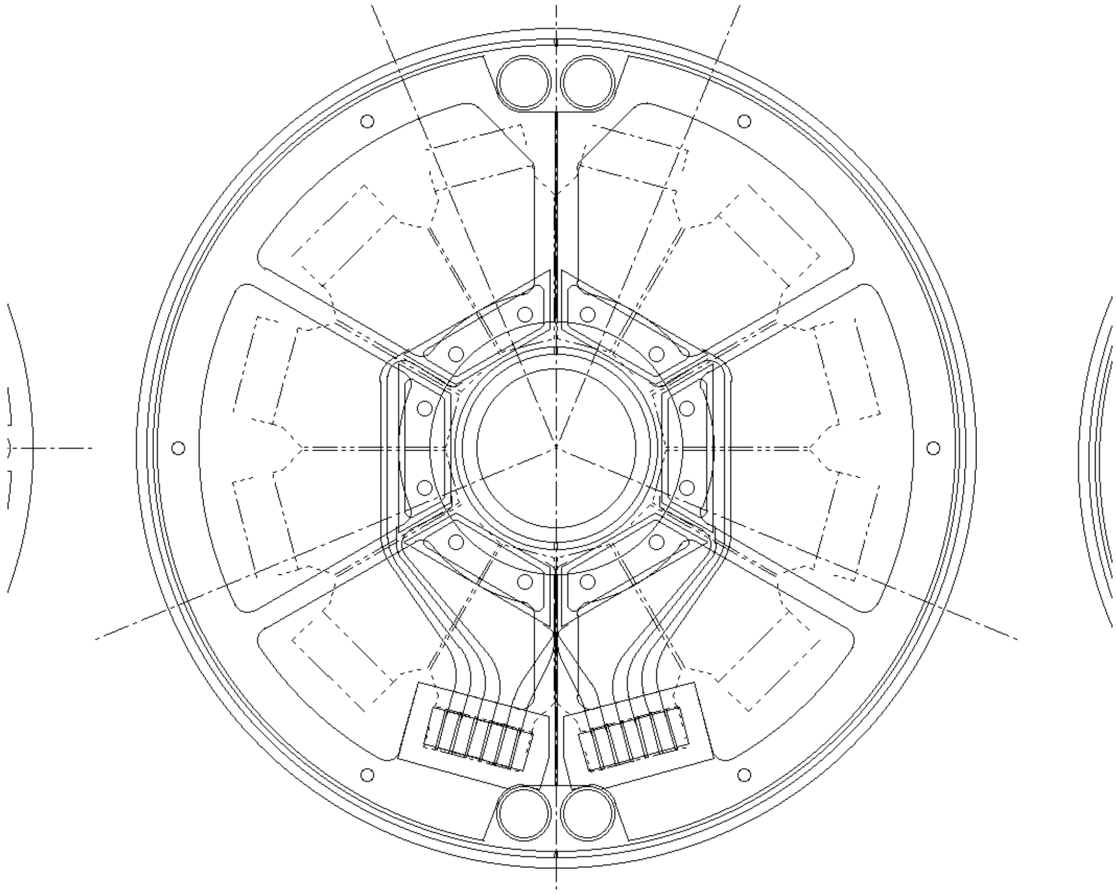

Figure 5.5: End view of the silicon enclosure showing the endcap, silicon pad motherboard with detectors and hybrid assemblies, and central barrel assembly with cables and plena.

The hybrid circuits are mounted to a support made of low-Z material to minimize the radiation length; we currently foresee using Rohacell foam for this. Besides supporting the hybrids, the support piece also forms a plenum to guide the cooling air. These plena provide the correct air flow geometry to allow near-laminar flow and isolate the cooling air from the rest of the MVD to minimize vibration effects. This is an important function, as the position stability of the hybrids is less critical than of the detectors. In this design, the air required to cool the electronics does not pass along the detectors. The detectors are only coupled to air flow- induced motion via the flexible kapton cables. Nevertheless, we are seeking to minimize the cooling air flow rates, and are performing R&D to measure the stability of the proposed structures with realistic air flows.

The plena, with hybrids attached, will be grouped together in each half-cylinder and enclosed to simplify the support and further channel the cooling air. A cross-section of this assembly is visible in Fig. 5.5. The assemblies are supported at both ends from the same support structure that holds the barrel azimuthal sectors. The geometry of this support scheme is illustrated in Figs. 5.4,5.3. If necessary, additional structural stability can be provided by tying the electronics package to the enclosure struts.

5.3.3 Cabling

The silicon strip and pad detectors are attached to the front end electronics on the hybrid circuits via custom designed kapton cables. These cables allow a physical distance between the silicon wafers and hybrids, providing thermal and mechanical isolation as described above. The updated electronics location is consistent with cable lengths of 20 cm or less, which have been shown to be acceptable by the L3 microvertex detector group. The cabling scheme is shown in Fig. 5.5.

With the new electronics location, particles pass through two cables in part of the electron arm acceptance. Consequently, it is crucial to minimize the radiation length of the cable. The kapton is 50 μm thick and aluminum, rather than copper, traces will be used. The STAR SVT group has had such cables fabricated, and found their performance adequate for analog signals [2]. The performance problems noted in those tests concerned high voltage on the cables, which is not an issue for the PHENIX MVD. We will perform extensive tests on prototype cables of this kind.

The cabling for the silicon pad wafers is more complicated, dictated by the geometry of the detector. The current conceptual design, as described in the CDR, involves a cable covering the entire detector surface, with holes for solder connections to each pad. An attractive alternative, which we are investigating with suppliers of silicon detectors, would use a double metallization layer to provide traces connecting each detector pixel to bond pads on one end of the detector wafer. This would preclude the need for the special kapton cable and allow wirebonding directly to the front-end electronics. We believe that the incremental cost of fabricating the pad detectors would be offset by savings in cable design and fabrication, and fewer wire bonds in the assembly stage.

5.3.4 Cooling

We have made extensive studies of air cooling the MVD, to take advantage of the low cost and minimal material in the path of the particles as well as eliminating potential coolant spills in the region of the silicon. The results of these studies are summarized in this subsection, along with progress in the conceptual design of the cooling system.

Each row of 12 barrel hybrid circuits is mounted to a structure forming a plenum to provide a path for the cooling air. The cross section of each plenum is 2.3-cm wide by 64-cm long, dictated by the size of 12 adjacent hybrids. The endcap hybrids are enclosed by a curved plenum, similar in aspect ratio. Each endcap plenum encloses six hybrids. The plenum depth is 6 mm, to maintain a plenum aspect ratio appropriate for maintaining laminar flow. Laminar flow is desirable to minimize vibration effects. However, our mounting scheme isolates the detectors from the cooling air and may allow us to relax this requirement in exchange for the improved cooling efficiency when the air flow is no longer laminar. This is being extensively investigated in the lab by measuring the cooling effectiveness and movement

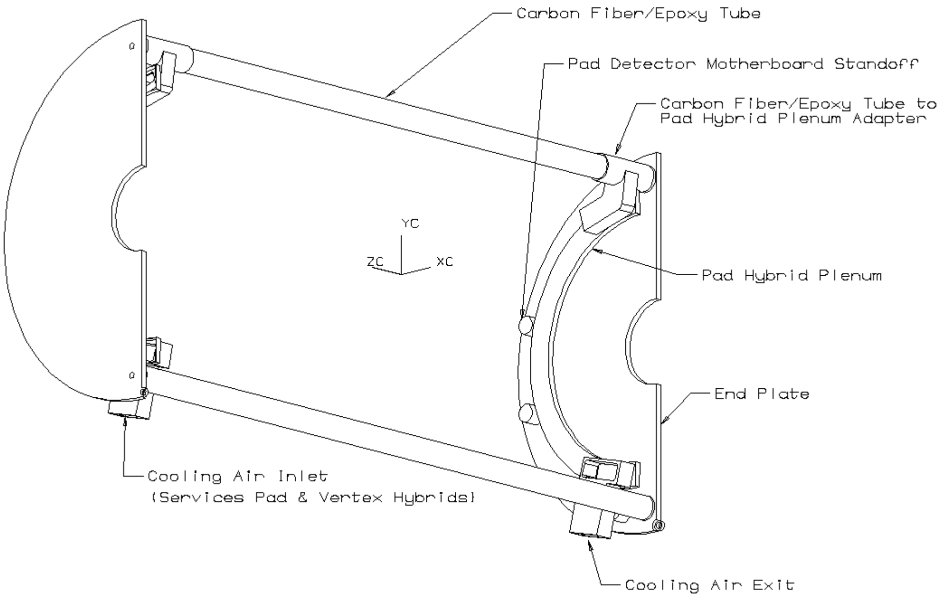

Figure 5.6: Cutaway view of the silicon support and enclosure showing the cooling air channels and the entry and exit path.

induced by various air flows in prototype plena. Air flows along one side of the hybrids only, as the other side is covered by polyimide, which has poor thermal conductivity.

Figure 5.6 shows the distribution system for the cooling air inside each enclosure half to supply the plena for the barrel and endcap silicon. The air is driven into the enclosure halves by a fan and heat exchanger located outside (we expect that this will sit at the bottom of the central magnet, below the detector active area). Air enters from one side, at the bottom of the enclosure, and is split into two streams. One stream flows through the group of plena holding the barrel hybrids, and the other passes through the half-circular plenum covering the endcap hybrids. This air then flows to the other side of the enclosure to cool the hybrids of the other endcap. The path from one side of the enclosure to the other is inside one of the graphite composite tubes serving as a structural strut, minimizing the material in the cooling system. After passing along the hybrids of the other endcap, the air then joins the barrel cooling air and exits the enclosure to be cooled and recycled, or vented outside of PHENIX.

The electronics on the hybrid circuits will dissipate 5 mW per channel, and there are 256 channels per hybrid; the total power dissipated is about 150 W. First tests of the prototype preamplifier lend confidence to this estimate of the power dissipation. The operating temperature must be maintained below 50 °C, where components fabricated in CMOS become temperature sensitive. The silicon wafers do not need cooling since they are physically separated from the electronics by the cable. The MVD outer enclosure provides humidity control to avoid any condensation problems on the detector wafers or other elements. We envision a low flow rate of dry nitrogen through the outer enclosure to provide this. The humidity control and isolation of the cooling air inside the plena make it possible to use chilled cooling air. This possibility gives a safety margin should the electronics power dissipation prove larger than currently estimated, or should we identify problems with the air flow rates described below.

The concept of air cooling the MVD was tested in the laboratory with a plenum made of phenolic (a paper/resin composite plus insulating foam). The thermal load of the electronics was provided by flat resistive heaters from Minco arranged in the geometry planned for the hybrids. A range of 2.5–18V powered the heaters to simulate heat loads around the expected 15W per plenum. Eight temperature sensors recorded temperature changes. Air was blown through the plenum with a fan, and the velocity measured with a flow meter.

These tests showed that an air flow rate of 14 mi/h keeps all the hybrids in a plenum at a temperature below 40 °C. The temperature increase from the first to last hybrid is only a few degrees Celsius, while the temperature increase of the cooling air is somewhat larger, but less than 10 °C. The temperature profile measured by the sensors along the plenum agrees reasonably well (within 10%) with calculations and indicates that the air flow is in the transition region between laminar and turbulent flow. The isolation of the cooling air inside the small plena, and the physical separation between the hybrids and detectors (linked only by the flexible kapton cable), mitigate the problems of detector vibrations from the air flow. The ruggedness of the hybrid fabrication implies that some motion of the hybrids should have no adverse effect on their performance. The magnitude of the hybrid motion is now being investigated using microaccelerometers.

We have also investigated the cooling of 10mW per channel, which results in 30 W per plenum. In this case, an air flow of 22.5 mi/h maintains the hybrids at 40–42 °C operating temperature. Another option, which we are currently studying in the lab, is to used chilled cooling air.

Another change from the CDR is that the elements of the first level trigger are now located outside of the silicon enclosure. The current sums from the hybrids can be driven far enough to allow this and significantly simplify the MVD cooling problem.

5.3.5 Assembly

Subassemblies are constructed by gluing and tab- or wire-bonding the kapton cables to the strip detectors. The detector/cable system is subsequently tested. The hybrid circuits should be independently mounted, and then connected to the cables. We are investigating the use of a connector consisting of a clamp and an elastomer strip which conducts in one direction only. Such elastomers have been successfully used at both LANL and BNL. The radiation length of the clamp required is of concern, so we are also looking into the possibility of using z-axis adhesive film for this connection.

The subassemblies are glued to the Rohacell, in subunits of the barrel. We are investigating azimuthal sectors which would be straightforward to install into the enclosure, but have the disadvantage of containing many permanently fixed silicon detectors. Another option is a half wheel-shaped subunit, which contains only 6 silicon detectors, but presents larger installation challenges. The endcaps will have the pad detectors and hybrids fixed to the motherboard, which is a much simpler assembly task.

It is clear that many fixtures will be required for alignment, assembly, testing and storage of detector/cable subassemblies and barrel subunits, as well as for the completed enclosures.

5.4 Electronics

5.4.1 Front end

Front end electronics design for the silicon detector systems is underway at Oak Ridge National Laboratory, supported by PHENIX R&D funds. A preamplifier/shaper chip has been fabricated using a CMOS process and has been shown to function. Several prototype chips have been shipped to LANL for wirebonding to a silicon strip detector and further testing. This chip will ultimately have 32 channels and a shaping time of 50–60 ns, though the prototype chip has five channels only.

As the silicon detectors provide a pulse height from each strip or pad, adequate pulse-height resolution is required to separate multiple charged particle hits on a single element. The dynamic range required is 4 mip and signal to noise of better than 10:1 for 1 mip. We are designing a circuit with a dynamic range of 8 mip to provide an adequate safety margin. A preliminary measurement of the electronic noise in the prototype preamp/shaper gives a signal to noise better than 12:1 for one mip with the capacitance of a silicon strip or pad.

The silicon detectors will provide information on the charged particle multiplicity for triggering via a sum of channels above threshold. The next version of the preamplifier (the true prototype) will provide a signal proportional to this. A current sum of the discriminator outputs from the eight preamplifier chips on each hybrid will be driven off the hybrid to the level-1 (LVL-1) trigger electronics for further manipulation. It has been shown that channels on a single silicon die in an ASIC are well matched in gain [3].

The analog memory unit (AMU) is a switched capacitor array with simultaneous read/write capability to pipeline the data pending a low level trigger decision. The MVD requires eight bits of resolution in the ADC to enable fitting the pulse height spectrum of the silicon pads. The MVD will use a variant of the AMU/ADC circuit under development for all of the PHENIX subsystems, modified for lower resolution and smaller power dissipation. Each channel has its own ADC circuit and a FIFO of at least two registers to store the data for readout. When an event is triggered, the information from the preceding beam crossing (which is very unlikely to contain a high multiplicity collision or particle hitting the same pixel) is used to set a reference level. The signal from the triggered event is compared to this reference to remove baseline shift and then digitized.

Control of the AMU, ADC and FIFO/readout is provided by a controller referred to in PHENIX as a “heap manager”. The heap manager for the MVD will be a variant of the one used by all PHENIX subsystems. Currently, it is foreseen that this function can be provided by a field programmable gate array. However, the MVD must use the heap manager as a bare die, whereas other subsystems can use the commonly available packaged modules. There will be one heap manager per hybrid to provide all necessary controls.

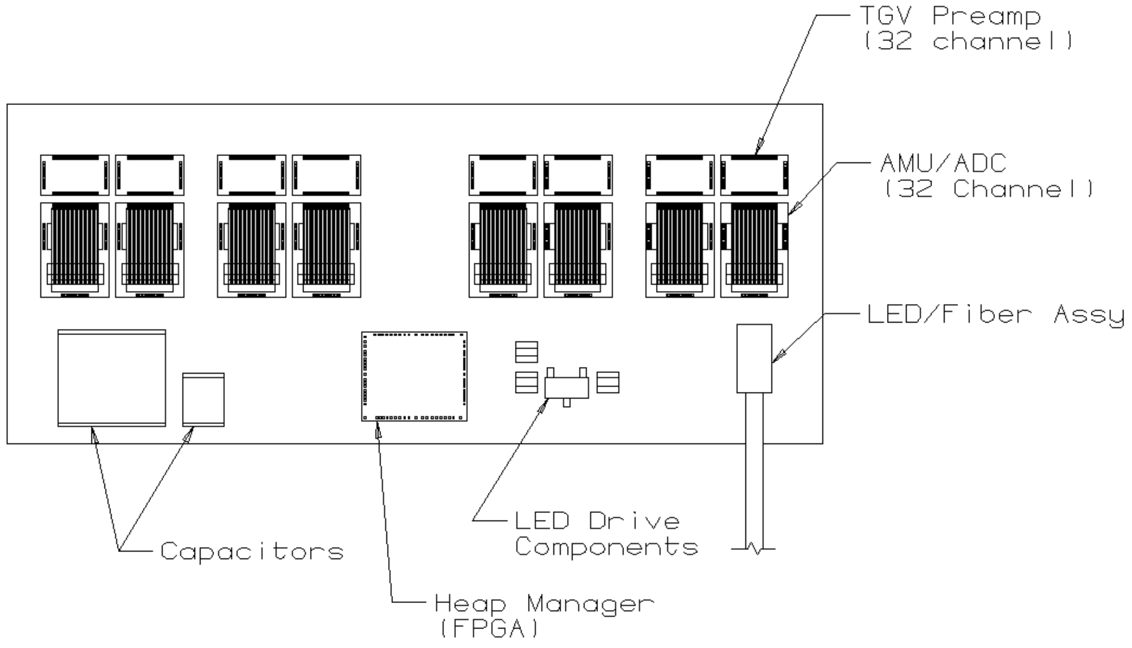

Figure 5.7: Layout of the hybrid circuit. The various components are labeled.

5.4.2 Hybrid circuit

Each detector wafer has 256 channels and is connected via a kapton cable glued and bonded to one hybrid circuit. This hybrid circuit has been simplified since the writing of the CDR by removing the zero-suppression and data packing functions. These will now be done on boards outside of the target region. All the information from a triggered event will be transferred off the hybrid via an optical link. A updated layout of the hybrid circuit is shown in Fig. 5.7. The signals enter the preamplifier/shaper/summer and then the AMU/ADC which both have 32 channels per die. Each hybrid also drives the current sum of the discriminator signals from the eight preamp/shaper chips to the LVL-1 trigger electronics. The 32 channels on each individual chip are summed on the chip. We expect that the driver will consist of surface mount components on the hybrid circuit and will not require an ASIC. The current hybrid circuit is 48-mm wide and 20-mm deep, fitting within the nominal mechanical constraints of PHENIX and other RHIC experiments as well.

The hybrid circuits will probably be fabricated using a process from Texas Instruments called High Density Interconnect (HDI). This process appears to be the best choice for the trace densities required in our circuit. Alumina substrates are used, with milled wells for the silicon dies. A polyimide coating is laser drilled at each die contact and then metallized to provide electrical contact and interconnect traces. This is a proven process that allows pitches of less than 100 μm. The high interconnect density is driven by the bus providing control signals (16×2 signals) from the heap manager to the AMU/ADC chips. The HDI process also offers the advantage of excellent thermal contact between the substrate and the

Table 5.2: MVD Material Thickness †

Source	$< X_0 >$ (PISA)	$< X_0 >$ (CDR Update)
Dalitz	0.61%‡	0.61%‡
Beam Pipe	0.28%	0.28%
MVD Layer 1	0.32%	0.32%
MVD Layer 2	0.32%	0.32%
MVD Electronics	0.52%	0.52%
Rohacell Support	0.003%	0.01%
Enclosure	—	0.08%
Kapton Cables	—	0.04%
Total	2.06%	2.18%
MVD/(Dalitz + Beam Pipe)	1.31	1.45
MVD/(Dalitz + Beam Pipe) - without electronics	0.73	0.87

† This table includes a full outer barrel of silicon detectors.
‡ Dalitz decay of π^0 expressed as an equivalent in radiation lengths contributing to background.

chips, to simplify the heat removal.

5.5 Silicon System Performance Issues

We have made detailed studies of the effect of the MVD on the rest of the PHENIX experiment using the PISA program as described in Chapter 3. The number of background electrons arising from the MVD and the effect of those on the electron trigger and offline electron analysis was discussed there. In this section we will describe studies specific to the layout and design of the MVD. Table 5.2 shows the radiation length of material in the current MVD design, and compares to what was included in the PISA calculations shown. About 10% of the material was not accounted for in the simulations, but this omission should not alter any of the conclusions.

5.5.1 Electronics Location

PISA was used to investigate the difference between the current MVD with the barrel electronics on the bottom and the CDR design with the electronics oriented radially, in three sections separated by 120° in azimuth. The new arrangement both reduces the background in the RICH and simplifies the cooling of the electronics. Table 5.3 Comparison of $e^{\pm}$ background from the barrel electronics in the CDR configuration and with all of the electronics on

Table 5.3: Comparison of the e$^{\pm}$ Background from the Barrel Electronics

Electronics Configuration	N/event (no cuts)	N/event ($p_T > 200$ MeV/c)
CDR	0.78 ± 0.12	0.38 ± 0.09
Bottom Only	0.63 ± 0.08	0.00 ± 0.00

the bottom of the detector; both calculations include a full outer silicon layer. Backgrounds are calculated using PISA, based on photons from π^0 decay in central Hijet events.

The calculations summarized in Table 5.3 assume a complete barrel detector without a hole in the upper two-thirds of the outer layer. With the CDR electronics configuration 0.78 ± 0.12 electrons originating in the electronics enter the RICH per event. This number falls slightly to 0.63 ± 0.08 per event with the electronics on the bottom. For electrons with $p_T > 0.2$ GeV/c, the difference is significant. In 100 simulated events, no electrons reach the RICH from the electronics when they are on the bottom. With the electronics configured as in the CDR 0.38 ± 0.09 electrons per event with $p_T > 0.2$ GeV/c reach the RICH. It is easy to understand why the p_T cutoff is so successful in eliminating background when the electronics are on the bottom. When a photon converts to an e$^{\pm}$ pair, the produced particles go approximately in the direction of the original photon, in this case, downward, away from the detector arms. Electrons with momenta significantly greater than the 100 MeV/c p_T kick from the central magnet cannot be bent the approximatiley 60° or more that is required for them to enter the RICH.

5.5.2 Silicon Coverage

The issues influencing the extent of silicon coverage in the MVD are electron background from photon conversions in the MVD material, and the competing requirements for good efficiency to find the vertex in low multiplicity events. It is clear that minimizing the background implies minimum material in the MVD, and maximizing vertex finding efficiency requires maximum coverage with two layers of silicon. The rapid changeover time between A + A and p + A running prohibits the solution proposed in the CDR of modifying the number of barrel azimuthal sectors in the MVD. We have used the PISA calculations to find an optimal solution between these two extremes.

To do this, we used the PISA simulation to study the effect of omitting silicon strip detector wafers from the outer barrel layer, along with the associated cabling and electronics. Making a hole in only one of the two layers preserves the possibility of triggering on multiplicity in the barrel in an unbiased way, and the ability to search for multiplicity fluctuations at midrapidity. Furthermore, this approach allows the remaining outer silicon to be useful for vertex finding. The vertex algorithm uses tracks which hit both silicon layers, but the overlap in η becomes small as the two layers become short in z, causing the number of useful tracks to fall drastically. However, leaving one layer complete in z means that whatever

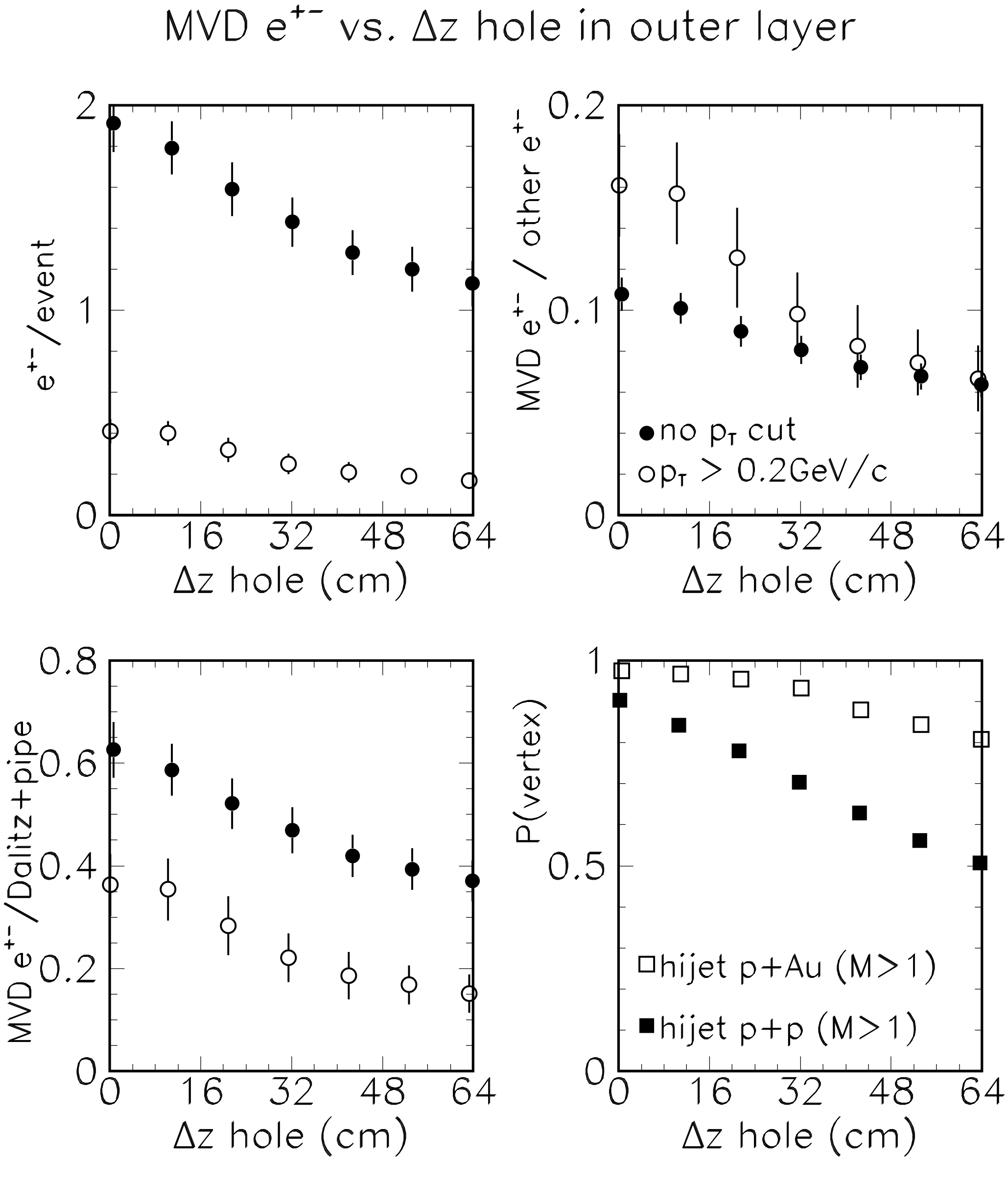

Figure 5.8: The electron background from MVD in central Au + Au collisions and the probability of finding the vertex in p + Au and p + p collisions, as a function of the amount of silicon removed from the top two-thirds of the outer barrel layer.

remains of the other layer contributes to the vertexing capability. This compromise avoids relying on the lower one-third of the barrel alone, which has been shown to yield only 50% vertex reconstruction efficiency for p + p collisions. One of the major issues addressed is whether the electron background is sufficiently low with this approach.

Figure 5.8 shows the results of this study. The electron background and vertex finding efficiency are plotted as a function of the size of the hole along the z direction created by omitting elements of the top two-thirds of the barrel outer layer. The top left shows the number of conversion electrons per event from the MVD which enter the electron arms. The filled circles show the total number of electrons, while the open circles give the number of electrons with $p_t > 0.2$ GeV/c. This p_T cut is roughly equivalent to the threshold imposed by the angular acceptance of the Winston cones in the RICH. Below this threshold, the electrons will not be identified by the RICH. It is clear that the majority of the MVD conversion electrons in the electron arm acceptance are very soft and are below this p_T threshold. The top right gives the fraction of MVD conversion electrons out of the total background electrons entering the RICH. This illustrates the magnitude of the MVD contribution to electrons at the trigger level. This fraction is quite small, independent of the p_T threshold. The bottom left shows the ratio of the MVD conversion electrons to those arising from Dalitz decays and conversions in the beam pipe (the irreducible electron background in the baseline PHENIX detector). This plot shows the increase in the background from the MVD expected in the offline analysis, and allows evaluation of the increase in the combinatorial background caused by material in the MVD. The right bottom shows the probability of finding the vertex position in p + Au and p + p events, also as a function of the hole size. It should be noted that this is for events which have at least two charged particles produced in the η range of the barrel.

By comparing the bottom two sections of Fig. 5.8 the tradeoff between background and vertex efficiency can be quantified. The background above p_T of 0.2 GeV/c is the relevant quantity for this comparison. The left side shows that with the entire outer silicon layer, the MVD increases the single electron background by one-third, and the dielectron combinatorial background by a factor of 1.75. An MVD with only one silicon layer in the top two-thirds increases the single electron background by about 20% and the combinatorial background by 40%. The collaboration agrees that we do not want to increase the combinatorial background by nearly two, but a 40% increase is acceptable. This implies a hole size of 40 cm or more in z. Inspection of the right bottom plot shows that the probability of finding the vertex is only 50% with no outer layer in the top two-thirds of the MVD, but improves to 65% with a 40-cm hole in that layer. Though this is not ideal for analysis of p + p collisions, the collaboration has decided to accept this as truly low multiplicity events have a high cross section and the rate loss should not preclude collection of sufficient statistics. The measurement of high mass dileptons, which have lower production rates, will be hurt by this efficiency loss if the dileptons arise from low multiplicity events or are accompanied by jets which can miss the two layer section of the vertex detector.

5.6 Cost and Schedule

The cost estimate and schedule for the MVD is presented in Table 5.4. In this table the MVD mechanical (WBS 5.2.1) and front-end electornics (WBS 5.3.1) cost are shown at PHENIX WBS level 4. The detailed cost estimate, along with the schedules and profiles, is available in the PHENIX WBS book. The dictionary, basis of estimate, and contingency analysis are presented in the PHENIX WBS Notes book.

Table 5.4: Cost Estimate and Schedule for the PHENIX MVD

WBS	Description	Total Cost
5.2.1	MVD	$1,262,298.00
5.2.1.1	Engineering & Design	$291,024.00
5.2.1.2	MVD Prototypes	$233,476.00
5.2.1.3	MVD Fabrication	$647,478.00
5.2.1.4	MVD Assembly	$42,640.00
5.2.1.5	MVD Testing	$47,680.00

WBS	Description	Total Cost
5.3.1	MVD FEE	$697,926.00
5.3.1.1	Engineering & Design	$229,216.00
5.3.1.2	MVD FEE Prototypes	$157,310.00
5.3.1.3	MVD Electronic Fabrication	$311,400.00

5.7 Beam-beam Counter Overview

The PHENIX beam-beam counter (BB) provides information for triggering on beam-beam collisions, the rough collision vertex position along the beam axis (z) that helps to find correlation between tracks in various detector elements, and the time origin of the collisions. The information must be available at the trigger level to discriminate backgrounds, and the timing information is also used to perform the time-of-flight measurement for particle identification combined with the information from the TOF detectors.

The BB consists of two arrays of counter elements, one each placed upstream and downstream of the beam crossing point. Each array consists of 66 modules of counter elements surrounding the beam pipe, and covers the forward and the backward rapidity regions. The average and the difference of the arrival times of fast leading particles from beam-beam collisions to the two BB counter arrays provide the time origin and the vertex position of the collisions, respectively.

Each counter element is constructed from a Cherenkov radiator of fused quartz and a 1-in. mesh-dynode photomultiplier made by Hamamatsu (Hamamatsu H5082). The fused quartz radiator is glued to the photomultiplier window. With such a combination of radiator and the photomultiplier, an intrinsic timing resolution of 44 ps was achieved for 1.6 GeV/c pions in a beam test at KEK. Good operation of the BB is expected in the magnetic field environment of the BB location due to the choice of photomultiplier.

The BB electronics chain consists of discriminators, shaping amplifiers, time-to-voltage converters (TVC), flash ADCs (FADC) and buffer memories. The timing and pulse height information of the BB elements are digitized in every beam crossing by the TVC and FADC. The digitized data are provided as a set of input of the LVL-1 trigger, and are stored at the same time in the buffer memory for the event building. The discriminators are designed so that the walk-free timing information from the BB is available in the LVL-1 trigger.

5.8 Beam-beam Counter Changes

Since the CDR, there has been considerable progress in the BB design. Based largely on the results of a beam test of counter elements, there are several changes and refinements, which include:

1. The selection of a hexagonal face, rather than circular face, as the shape for the front of the BB counter elements.

2. The change in design of the counter elements of the BB to minimize radiation damage.

3. The development of a new method for maintainence access to the BB detector on the muon arm side to reduce interference with access to the muon arm and central magnet.

4. The investigation and testing of a candidate for the BB discriminator, based on the double threshold method.

Performances of Cherenkov radiators with a hexagonal and a round cross-section for the shape of the BB counter elements were compared in a beam test at KEK. Round Cherenkov radiators with different lengths and diameters were also tested to optimize the radiator size. The shape (hexagonal) and size (29×30 mm^2) of the Cherenkov radiator for the BB counter elements were finalized by the beam test.

The BB location is a high radiation environment in the PHENIX detector. Though the estimation of the radiation level at the BB location is still under way, it is obvious that the BB detector requires good radiation hardness. The radiation hardness of photomultipliers and Cherenkov radiator materials against neutrons and γ-rays was considered, and the design of the counter elements of the BB was changed to minimize the damage of the radiation. Furthermore, the BB location is also a high counting rate environment. Together with the radiation damage, a deterioration of photomultiplier tubes by an over current in the dynode chain, caused by the high rate counting, possibly contributes to the damage of the BB counter elements. An averaged current in the dynode chain was estimated and was compared with the critical current of the photomultiplier tubes.

The BB counter array at the muon spectrometer side will be installed into a space between the central magnet and the muon tracking chambers. The maintenance access to the BB detector is not straightforward. The access inevitably interferes with the central magnet and the muon chambers. The method of the maintenance access to the BB detector at the muon spectrometer side was changed to reduce the interference.

An important requirement of the BB counter is to provide timing information of good quality to the LVL-1 trigger. For the requirement, the discriminator of the BB counter must provides walk-free timing information in the high multiplicity environment. A candidate of the discriminator based on the double threshold method was tested.

5.9 Mechanical

5.9.1 Detector Elements

Each element of the BB counter is a flashlight-type Cherenkov counter, with a UV-transparent solid Cherenkov radiator mounted directly on a mesh-dynode photomultiplier tube.

There were two options for the sape of the front face of the Cherenkov radiator shape: a hexagonal or a circular cross-section. Performance of the two Cherenkov radiator shapes was studied in a beam test at KEK. In the test, radiators of both shapes had comparable intrinsic timing resolutions. Consequently, the choice of shape is not determined by the intrinsic timing resolution. The hexagonal shape was chosen for PHENIX to minimize insensitive gaps between counter elements. The outer diameter of the hexagonal cylinder is 29 mm, which matches the 1-in. photomultiplier tube, and the length is 30 mm, which is the minimum length giving enough Cherenkov light to achieve a 50 ps intrinsic timing resolution.

It is known that the major radiation damage of photomultiplier tubes by neutrons and γ-rays is deterioration in the optical transparency of the window material, especially at short wave lengths. Such deterioration at short wave lengths is, of course, critical for Cherenkov counters. Deterioration in the transparency is lower for fused quartz than for normal and UV glasses. The fused quartz is accordingly a good choice for the Cherenkov radiator and window material. In the previous design of the BB counter elements, the radiator and photomultiplier were glued together, however glues have notoriously poor radiation hardness qualities. Therefore, a mesh-dynode photomultiplier with a thick fused quartz window, which is the Cherenkov radiator at the same time, of a hexagonal cylinder shape is newly designed by Hamamatsu, as shown in Fig.5.9. A 1-in. mesh-dynode photomultiplier based on the Hamamatsu H5082 is used. Similar to the Hamamatsu H5082, this new mesh-dynode photomultiplier is expected to work without a magnetic shield in the magnetic field environment at the BB location (see Fig.5.10).

Another factor of deterioration in the counter performance is an over current in the dynode chain of the photomultiplier tube. A damage by the over current lowers the current gain of the photomultiplier. In a high rate and high multiplicity environment, the deterioration determines the life time of the photomultiplier and the cycle of maintenance access needed to keep the BB performance. The deterioration comes from a thermal damage of the dynodes. The critical anode current is given as an averaged current over a few seconds, and its catalog value is 10 μA for the Hamamatsu H5082 photomultiplier. An estimated anode current I_{anode} of the photomultiplier tube in the Au + Au collisions at a luminosity of $2.2 \times 10^{27}\mathrm{cm}^{-2}\mathrm{s}^{-1}$

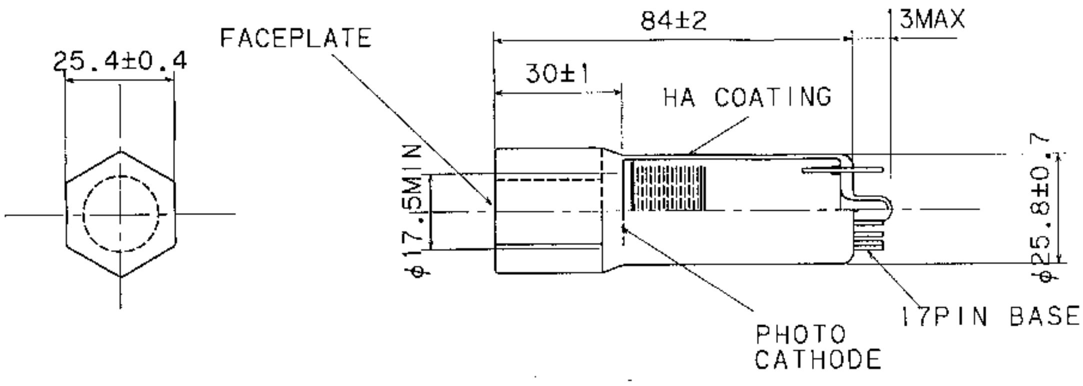

Figure 5.9: A 1-in. mesh-dynode photomultiplier newly designed by Hamamatsu based on the Hamamatsu H5082 The photomultiplier has a fused quartz window or radiator of hexagonal cylinder shape, a 29-mm outer diameter and a 30-mm thickness.

is:

$$I_{\rm anode} = 1 \times 10^{-10}{\rm C/mip} \times 2{\rm mips/event} \times 14 \times 10^3{\rm events/s} = 2.8\mu{\rm A}$$

.

In performing this calculation, we assumed that the integrated charge of the photomultiplier tube signal by a minimum ionizing particle (mip) is 1×10^{-10}C/mip, that the average number of mips in a counter module per event is 2 mips/event, and that the event rate is 14×10^3events/s. The resulting average anode current $I_{\rm anode}$ is below the critical value. At much higher luminosity, $I_{\rm anode}$ is likely comparable with the critical current. A reduction of $I_{\rm anode}$ by a factor of two is possible by reducing current gain of the photomultiplier tube without significant growth in the timing resolution. The study on effects of the over current in a realistic condition is still under way.

5.9.2 BB Location

The BB detector consistes of two arrays of the counter elements. Each BB array has 66 modules of the counter element. One BB array at the muon spectrometer side is located in the copper plug attached to the central magnet. Another BB array of identical assembly is mounted on a support stand at the other side.

In the previous design, the copper plug at the muon spectrometer side consisted of three parts, one cylindrical part covering the beam pipe and two tapered parts covering the BB. The copper plug was attached to the iron piston of the muon magnet. The maintenance access to the BB was possible only after removing several muon tracking chambers and the tapered part of the copper plug.

In the present design, the copper plug has a simple tapered shape and a maintenance access to the BB is possible from the rear side (see Fig.5.11). The access can be made by

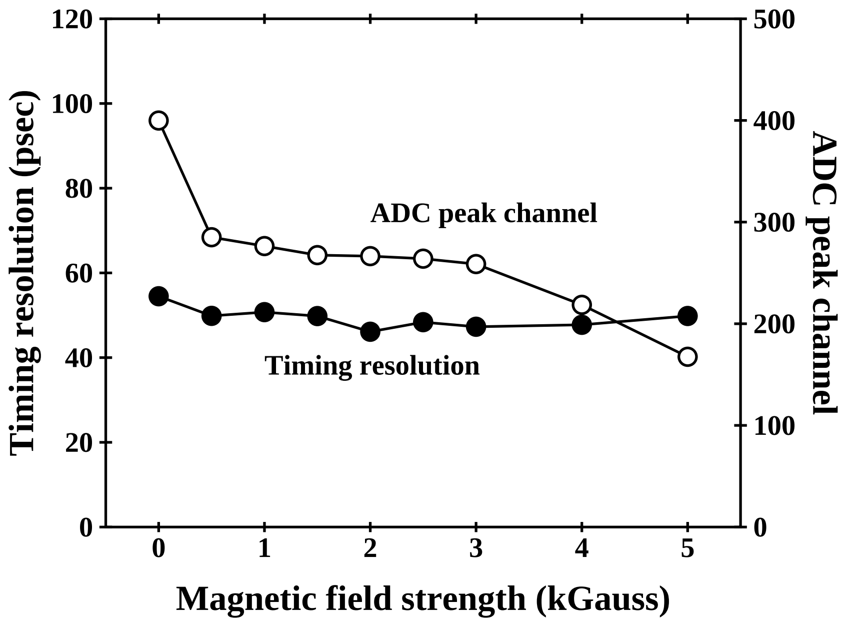

Figure 5.10: The dependence of the signal pulse height (filled circle) and the intrinsic timing resolution (open circle) on an axial magnetic field strength is shown for a combination of a hexagonal cylinder shape radiator and the Hamamatsu H5082 photomultiplier tube. The magnetic field strength at the BB location is expected to be less than 3 kG.

moving the central magnet away from the muon spectrometer. The BB, the copper plug, and the γ-ray absorber for the muon spectrometer are moved with the central magnet. The BB array is accessed from the rear side by a person standing at a 150-cm gap between the γ-ray absorber and the muon tracking chamber station #1, after the CM is moved away.

In accordance with the change of the copper plug design, cabling and cooling of the BB array at the muon spectrometer side was changed. Sixty-six coaxial signal cables, 11 high voltage cables, and 66 optical fiber cables, for counter calibrations, are laid through a 5-cm gap between the γ-ray absorber and the muon tracking chamber. The number of high voltage cables was increased from nine to 11 to keep the total current per high voltage cable less than 1 mA. The main heat source of the counter array is the bleeder circuit of the photomultipliers tubes. Total power consumption of the photomultiplier tubes in each BB array is $0.37 \times 66 = 24.4$W. The heat production of the BB is small enough to be cooled by fans. Furthermore, the circulation of air between the inside of the copper plug and the atmosphere is improved.

5.9.3 Electronics

In central Au + Au collisions, each counter element of BB is likely to be hit by multiple particles. The timing signal arises from the first particle entering the element, but the measured pulse height includes all particles, so traditional slewing correction is not applicable

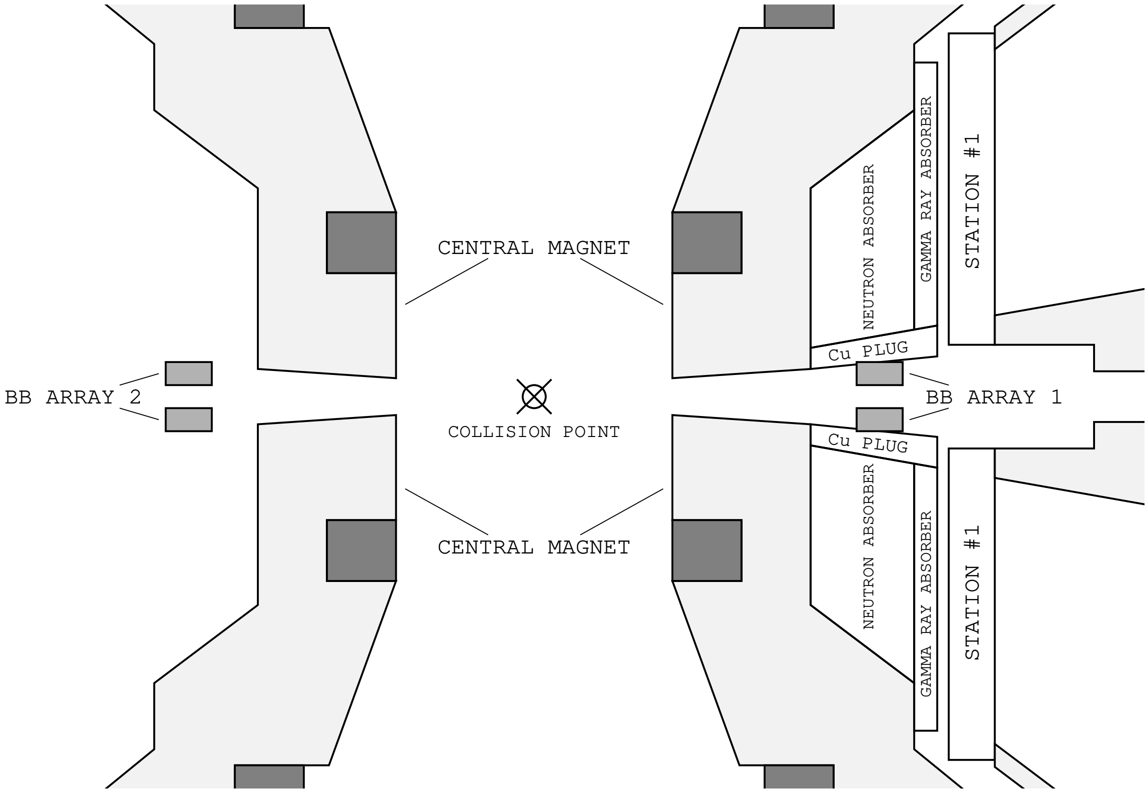

Figure 5.11: One BB counter array in the muon spectrometer side is installed to the inside of the copper plug. Another array is located at the other side of the central magnet.

at all. We will address this problem by using either a discriminator based on the double threshold method or a constant fraction discriminator (CFD).

The double threshold method uses two leading-edge discriminators with different thresholds. Two timing information T_1 and T_2 from the two discriminators are combined to get a walk-free timing information T_0 as follows.

$$T_0 = 2 \times T_1 - T_2$$

The two timings T_1 and T_2 are determined by the pulse shape at the leading-edge, at which the contribution of the first particle is dominant, and no pulse height information is needed to obtain the walk-free timing T_0. A merit of the double threshold method is that the method is based on the well established leading-edge discriminators. Another merit is that the on-line correction of the timing by the double threshold method is simple and is possible with no help of CPU. The feasibility of the double threshold method with ordinary discriminators was tested with 1.6 GeV/c pion beams at KEK, and we achieved 47 ps intrinsic timing resolution, which was comparable with a timing resolution by a leading-edge discriminator with applying the slewing correction.

The CFD might also provide walk-free timing information for the multiple particles. The development and testing of the CFD for PHENIX is still under way at LANL, and, at present, the final choice of the discriminator scheme is still open.

5.10 Beam-beam Counter Performance Issues

As indicated previously in Chapter 3, the beam-beam counter determines the time zero (T_0) when an interaction occurs in a beam bunch crossing (2 ns traversal time) and provides the first estimate of the vertex point (z_0) along the beam axis. The BB consists of two sets of identical counter arrays installed on both sides of the interaction region. One set is in the muon plug on the muon detector side, and the other is in free space just behind the central magnet yoke. These counter arrays intercept particles emitted at very forward angles in the rapidity range from three to four at $z = \pm 150$ cm. Charged particles with a velocity faster than $\beta = (1/1.458)^1 = 0.69$ will be detected by the counters. By measuring a pair of arrival times T_1 and T_2 of the fastest particle that intercepts the counter array on each side, T_0 and z_0 will be obtained as the average and the difference of T_1 and T_2, respectively.

If there were no backgrounds nor any slow particles, the resolutions of the extracted T_0 and z_0 would be affected only by the intrinsic time resolution of the counter elements. However, all interactions do produce slow particles, even at very forward angles, and there does exist a significant amount of background particles scattered from the central spectrometer structures and from the Muon detector. Therefore an examination of the BB performance with a Monte Carlo simulation is mandated.

The first results of the effects of the QED pair background have already been discussed in Chapter 3. Here we focus on evaluating the intrinsic performance of the BB counter arrays, in particular the simulation of the T_0 measurement. Those simulations have been carried out with an input of the geometry of the BB, as described in the PHENIX baseline design, and taking the intrinsic time resolution of each counter element to be 50 ps, and then using this information in the PISA/PISORP program chain.

The spectrometer components along the beam axis (i.e., the central magnet, beam pipe, nose cone, muon plug, and the muon piston) as well as the BB were installed in the PISA simulation to study the performance of the T_0 measurement under the realistic condition of background particles scattered from those materials in a magnetic field. Subsets of the PISA UA1-type events were thrown from the $z = 0$ position into a forward cone of polar angle 10°. The BB acceptance covers from 2° – 6°. The mean multiplicity of particles thrown within the cone was 100, and the BB detected about ten charged particles in average per event.

The PISA simulation returns several kinds of variables relating to the hit time, position, and direction of each charged particle which entered the sensitive volume of a given detector element. The simulation program also provides the amount of energy loss and the path length for each particle whether it has stopped in the detector element or entered and exited. The event contains not only leading particles from the vertex but also shower particles created by the leading particles both inside and outside the sensitive volume. All of this information is retained in the PISA output file for subsequent diagnostic analysis.

[1] The refractive index of quartz, which is the sensitive material of the counter elements.

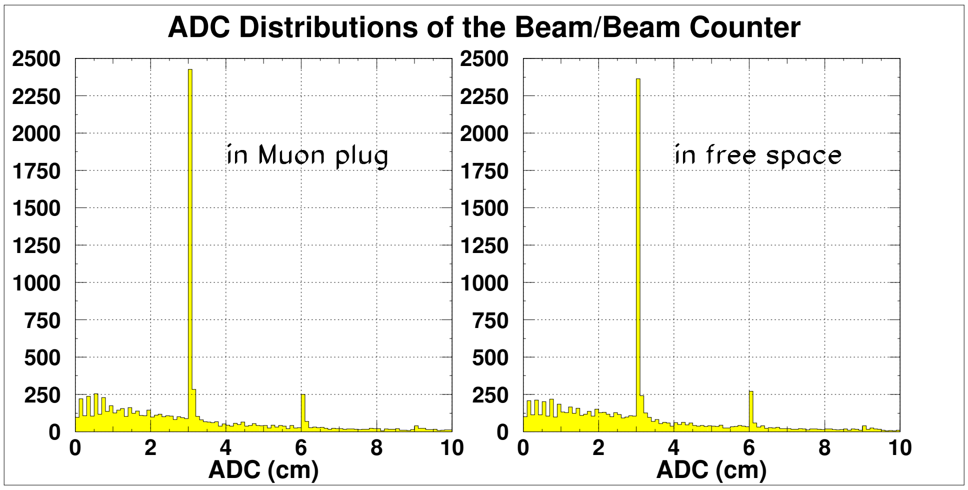

Figure 5.12: Simulations of ADC distributions of the BB detector system for 1000 UA1 type events. The left figure is for the detector elements on the muon arm side, and the right figure is for the detector elements on the free space side.

This output file is "played back" by the PISORP program in order to obtain the arrival hit times of all the particles in each event. The earliest time in each detector was defined to be the TDC data of the detector. The energy loss itself does not directly afford any signal information by the detector because it is a Cherenkov device. Instead, and in a manner somewhat akin to the simulation of the RICH counter, the ADC data for each BB detector element was taken to be the sum of the track lengths of all particles which have incident velocities above the Cherenkov threshold and whose directions are within a specified acceptance angle of 45°. (The RICH simulation goes one step further in that for tracking and timing purposes it generates Cherenkov photons and follows through their trajectories.) The ADC spectrum in Fig. 5.12 has a sharp peak at 3 cm, since the current design has a sensitive volume 3-cm thick and no smearing effects were included for the ADC response. The peak has a small tail on the high side due to secondary particle production inside the sensitive volume. Double hits in a single detector element result in a peak at 6 cm. The ADC simulation data show a large and continuous component over the full range. The region below the first peak represents events for which there were no leading particle hits but there was only a soft background of particles scattered from material outside the detector. The left figure is of the detector residing in the muon plug on the muon arm side, while the right figure is of the detector situated in free space. No noticeable yield differences in the backgrounds are apparent.

The two left figures in Fig. 5.13 show distributions of TDC data of all tracks recorded by the counter elements for 1000 events. The top figures are of the detector in the muon plug on the muon detector side, and the bottom are of the detector in the free space. The width of the both distributions is around 60 ps, and is wider than the intrinsic time resolution of the counter elements. This broadening occurs because the distribution contains TDC data of

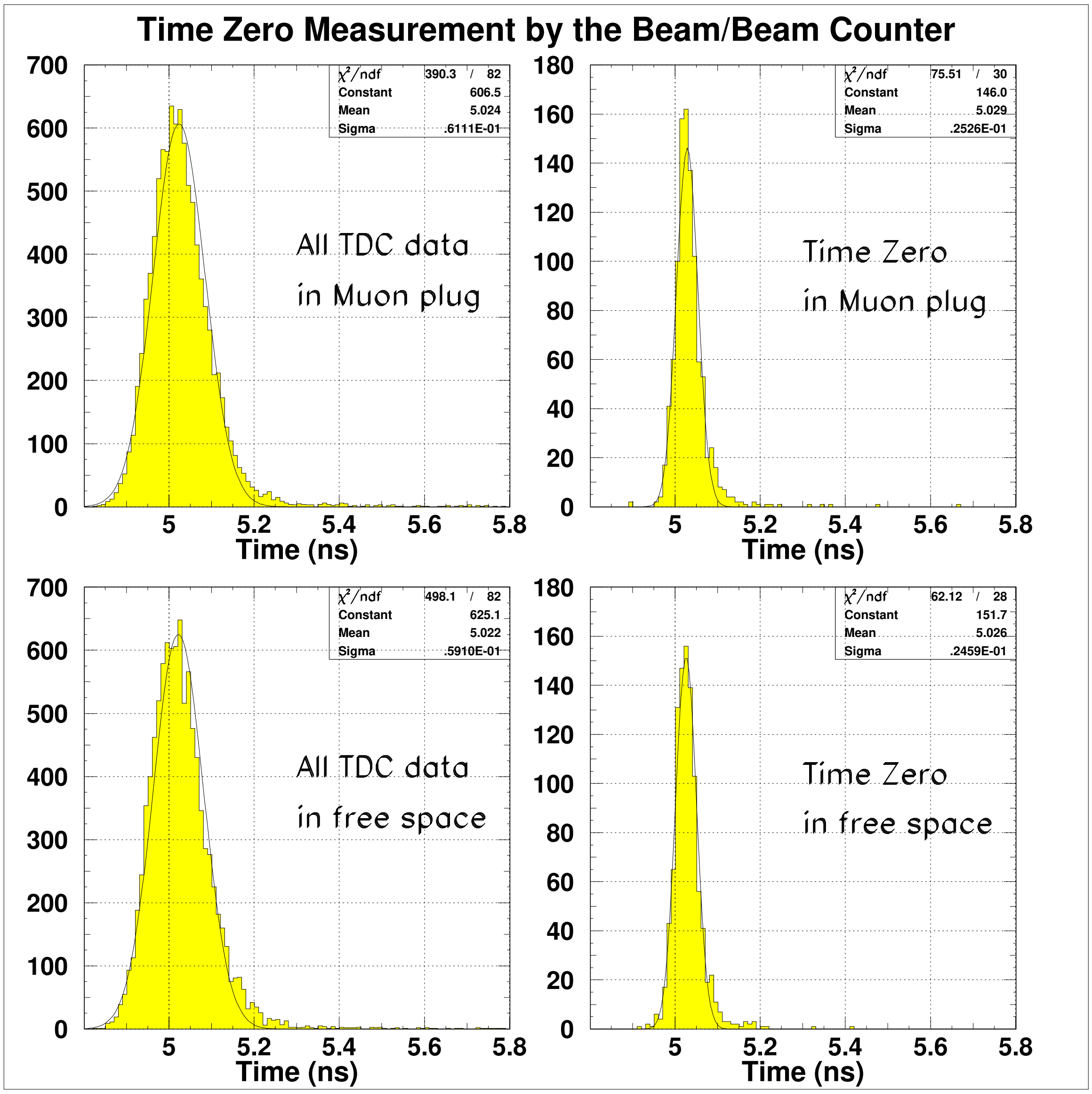

Figure 5.13: TDC distributions (left) of all tracks recorded by counters for about 1000 UA1 sub-events and the T_0 distributions (right) determined for each event. Top figures are of the BB in the muon plug on the muon detector side, and the bottom figures are of the BB in the free space on the opposite side. No significant differences are seen, although the two background environments are quite different.

slow particles and of background particles that are produced in the magnets and absorbers and arrive at later times.

The T_0 of each event is determined from TDC data recorded in the event. In this simulation, the T_0 was obtained by taking a simple average of the TDC data of the event. The right two figures in Fig. 5.13 show distributions of the T_0. The resolution was found to be about 25 ps, being better than the intrinsic counter resolution on account of multiple measurements of the arrival time. It is noteworthy that there is no difference of the spectral shape or the width between the spectra of the one set of BB counters placed in the muon plug and the other set in the free space, even though the background fluxes around the detectors are certainly different.

5.11 Cost and Schedule

The cost estimate and schedule for the BB counter is presented in Table 5.5. In this table the BB mechanical (WBS 5.2.2) and front-end electornics (WBS 5.3.2) cost are shown at PHENIX WBS level 4. The detailed cost estimate, along with the schedules and profiles, is available in the PHENIX WBS book. The dictionary, basis of estimate, and contingency analysis are presented in the PHENIX WBS Notes book.

Table 5.5: Cost Estimate and Schedule for the PHENIX BB Counter

WBS	Description	Total Cost	No
5.2.2	BB	$512,232.16	
5.2.2.1	Prototype Testing	$40,881.92	
5.2.2.2	Fabrication	$393,110.24	
5.2.2.3	Testing	$21,040.00	
5.2.2.4	Cables	$8,400.00	
5.2.2.5	Installation	$48,800.00	

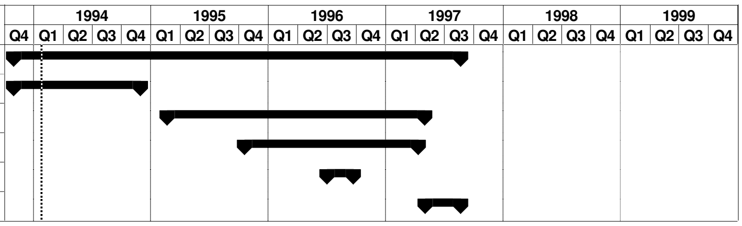

WBS	Description	Total Cost
5.3.2	BB_FEE	$169,511.60
5.3.2.1	Design	$48,000.00
5.3.2.2	Prototype	$15,180.80
5.3.2.3	Modification	$19,200.00
5.3.2.4	Fabrication	$79,450.80
5.3.2.5	Installation	$7,680.00

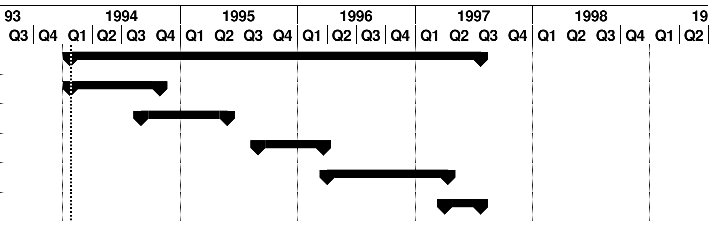

Bibliography

[1] J.P. Sullivan, et. al, Proceedings of the Symposium on RHIC Detector R&D, BNL-52321, p.107 (1992).

[2] R. Bellwied, private communication.

[3] C.L. Britton, Jr., G.T. Alley, M.L. Simpson, A.L. Wintenberg, R.J. Yarema, T. Zimmerman, J. Boissevain, J. Simon-Gillo, J.P. Sullivan, B.V. Jacak, and N. Lockyer, submitted to IEEE Nuclear Science Transactions.

Contents